Chapter 6

Static Soft Tissue Prediction

In this chapter, the results of experimental investigations carried out with artificial objects as well as with the geometric models of real patients derived from tomographic data are presented. Some general aspects of the FEM modeling of deformable objects can be gathered by studying simple artificial objects being under the impact of predefined loads. We focus on the comparison of the numerical results with the theory, the effects of the mesh refinement as well as the comparison between the linear and non-linear elastic approaches. Finally, we apply our approach for the prediction of the patient's postoperative appearance in the surgical planning of large and small bone rearrangements.

6.1 Experiments with Artificial Objects

The experiments with artificial objects are carried out (i) to compare the result of the finite element simulation with the theory, (ii) to quantify the difference between the linear and non-linear elastic approach and (iii) to validate the advanced modeling techniques with simple 3D objects.

Linear elastic model. In order to validate the numerical simulation of the object deformation, one ideally needs a closed-form solution of the given problem. Unfortunately, there are very few examples of closed-form solutions in three-dimensional structural mechanics. One of such closed-form solutions is the so-called *fundamental solution* of the Lamé-Navier PDE, which describes the deformation of an infinitely extended linear elastic medium under the impact of the Dirac-delta distributed force density, see Appendix A. The fundamental solution yields the deformation (the displacement field) for every point of infinite mechanical continuum as a function of coordinates $\mathbf{u}(\mathbf{x})$. An infinitely extended medium Ω_∞ cannot be trivially discretized by finite elements. However, an arbi-

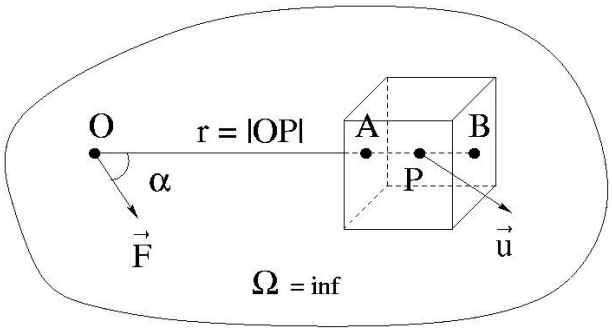

Figure 6.1: Cubic subdomain of infinitely extended elastic continuum being under the impact of the force density applied at the point O.

trary shaped subdomain $\Omega \subset \Omega_\infty$ can be understood as a separate elastic body with constraints given on its boundary by the prescribed displacements of all surface points $\forall \mathbf{x}\,, \;\; \mathbf{x} \in \Gamma \subset \Omega$. Consider a cubic subdomain of Ω_∞ as shown in Figure 6.1. The force applied at the point O generate a displacement field in the whole domain Ω_∞. Since the fundamental solution for the Dirac-delta distributed force density (A.2) is singular in the source O, we use the singularity-free solution derived for the Gauss distributed force density (A.5), which predicts theoretical displacements of both boundary and inner points of the test cube $\mathbf{u}_T(\mathbf{x}) \;\; \forall \mathbf{x}\,, \;\; \mathbf{x} \in \Omega$. Further, in accordance with the *Somigliana's identity* [8]: the displacement of an arbitrary inner point P of a homogeneous linear elastic domain is uniquely described by the boundary displacements $u_i(Q)$ and tractions $t_i(Q)$

$$u_i(P) = \int\limits_\Gamma u_i^*(P,Q) t_j(Q) dS - \int\limits_\Gamma t_i^*(P,Q) u_j(Q) dS \; . \tag{6.1}$$

Thus, we can formulate the following boundary value problem for the discrete domain Ω_N:

Compute the displacements of inner nodes $\mathbf{u}_N(\mathbf{x}) \;\; \forall \mathbf{x}\,, \;\; \mathbf{x} \in \Omega$ *for the prescribed boundary displacements* $\mathbf{u}_N(\mathbf{x}) \;\; \forall \mathbf{x}\,, \;\; \mathbf{x} \in \Gamma$.

Consequently, the results of the FE simulation $\mathbf{u}_N(\mathbf{x})$ for inner nodes of the cube $\forall \mathbf{x}\,, \;\; \mathbf{x} \in \Omega$ have to be compared with the theoretically predicted displacements $\mathbf{u}_T(\mathbf{x})$ for these nodes.

This strategy is applied in conjunction with the verification of the domain refinement. For this purpose, we consider four levels of uniform refinement of the

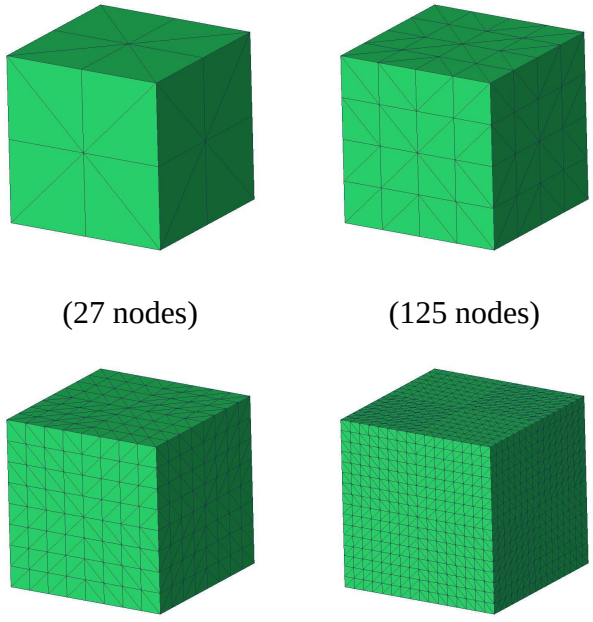

Figure 6.2: Uniform refi nement of cubic domain.

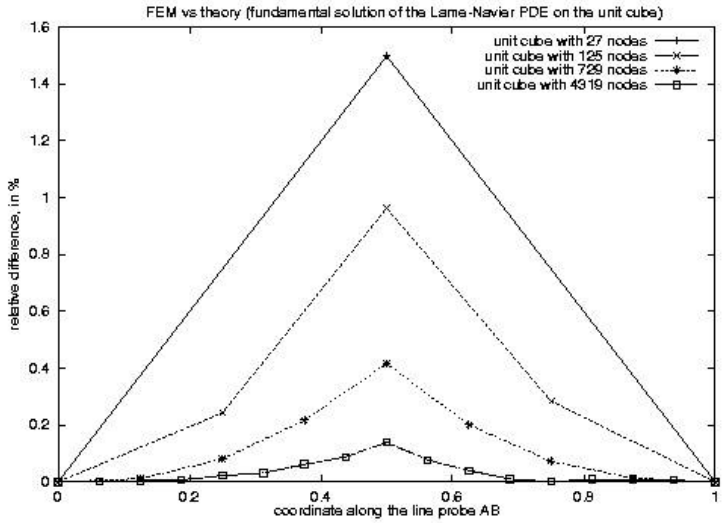

Figure 6.3: Comparison between the FEM solution and the theory along the line probe AB (Figure 6.1) for different levels of domain discretization (Figure 6.2).

cubic domain (see Figure 6.2):

0-level (initial discretization): 27 nodes (48 tetrahedra),

1-level: 125 nodes (384 tetrahedra),

2-level: 729 nodes (3072 tetrahedra),

3-level: 4913 nodes (24576 tetrahedra).

The comparison is carried out as follows:

1. First, the theoretical displacement $\mathbf{u}_T$ for N points of the cube are calculated by setting their coordinates in (A.5). The material properties are defined with $rE = 1$ and $\nu = 0.4$. The direction of the force $\mathbf{F}$ is set along the line probe AB, i.e. $\alpha = 0$, cf. Figure 6.1.

2. Then, the displacements $\mathbf{u}_N$ of inner nodes of the cube with the same material properties are computed via the linear elastic FEM for the boundary conditions given by the prescribed displacements of surface nodes as described above.

3. The relative difference $|\mathbf{u}_T - \mathbf{u}_N|/|\mathbf{u}_N|$ for each node along the line probe AB (see Figure 6.1) is measured.

In Figure 6.3, the results of this comparison are shown. The effect of the domain refinement is clearly seen in the reduction of the numerical error by factor 2 as predicted by the theory. The maximum relative difference between the FEM and the theory in this example amounts up to 1.5%.

Linear vs non-linear elastic model. The comparison between the linear and non-linear elastic approach is carried out with a simple artificial model consisting of a cylindric object with isotropic and homogeneous material properties, see Figure 6.4 (a). The boundary conditions are given by the prescribed displacements at the top of the cylinder, see Figure 6.4 (b). The associated boundary value problem is solved both by applying the linear and non-linear elastic FEM, see Figure 6.4 (c,d). It can be seen that the non-linear calculation yields significantly smaller displacements in comparison with the linear one, which is the direct result of the higher "geometrical stiffness" predicted by non-linear elasticity. In Figure 6.4 (e), line probes for the linear and non-linear solution measured along the main axis of the cylinder are depicted. The linearization error in this example reaches the maximum value on the boundary and amounts up to about 20 percent!

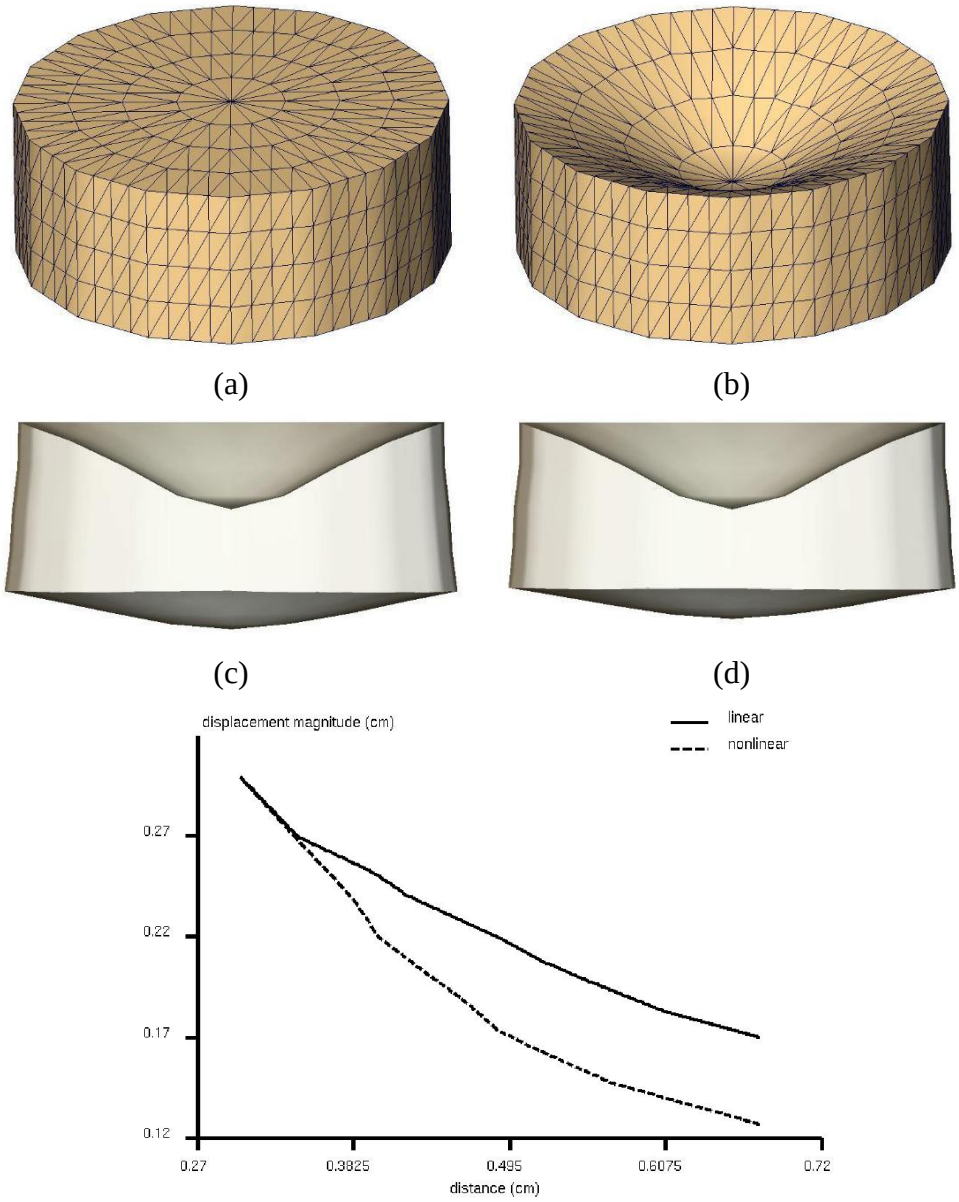

Figure 6.4: (a): undeformed cylindric object, (b): boundary conditions on the top of the cylindric object, (c,d): comparison between the linear and non-linear elastic deformation of a cylindric object, (e): line probes for the linear and non-linear deformation measured along the main axis of the cylinder.

Convergence behavior in dependence on ν. The Poisson ratio is the critical parameter of the pure displacement FEM. When the Poisson ratio approaches 0.5, the condition number of the stiffness matrix rapidly increases and the convergence of the PCG method becomes extremely bad. In Figure 6.5, the number of PCG iterations required to achieve the predefi ned precision of the solution in dependence on the Poisson ratio is shown. This diagram shows that convergence rate of the PCG method becomes extremely worse for $\nu > 0.45$. Thus, we consider $\nu = 0.45$ as an admissible upper threshold for the approximation of a quasi-incompressible material via the pure displacement FEM.

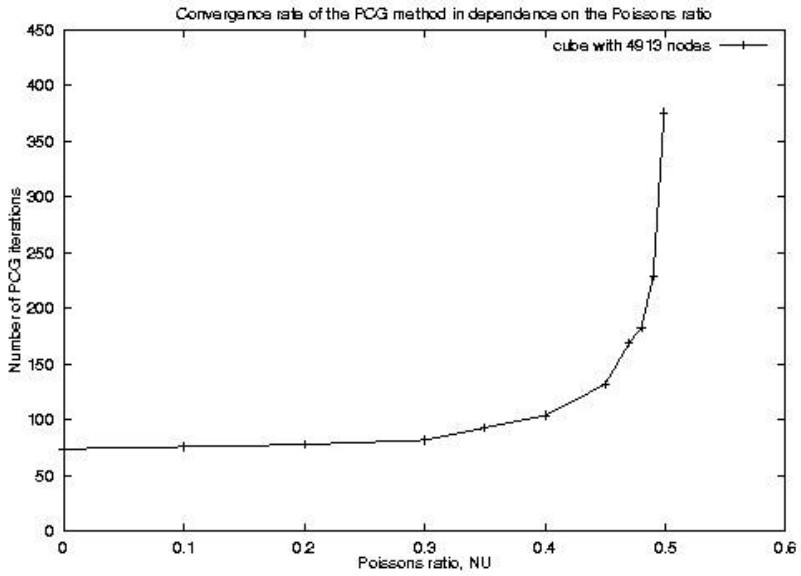

Figure 6.5: Convergence rate of the PCG method as a function of ν.

Sliding contact modeling. Besides the essential and natural boundary conditions (BC), special boundary constraints arise in the soft tissue modeling. For instance, contacts between lips and teeth, skin and muscles appear as a kind of sliding. Sliding can be modeled as the homogeneous essential BC with respect to the local surface normal. To demonstrate the effect of sliding, following experiment is carried out. We consider a cylindric object under the impact of the force density acting across the XY-plane from "north-west" to "south-east", see Figure 6.6 (top). The top of the cylinder is fi xed. In Figure 6.6 (middle), the deformation of the cylinder with the natural BC on the remaining boundary is shown. Figure 6.6 (bottom) illustrates the deformation with the sliding contact constraint $\mathbf{u}(\mathbf{x})^{\mathbf{T}}\,\mathbf{n}(\mathbf{x}) = \mathbf{0}$ at the cylinder bottom.

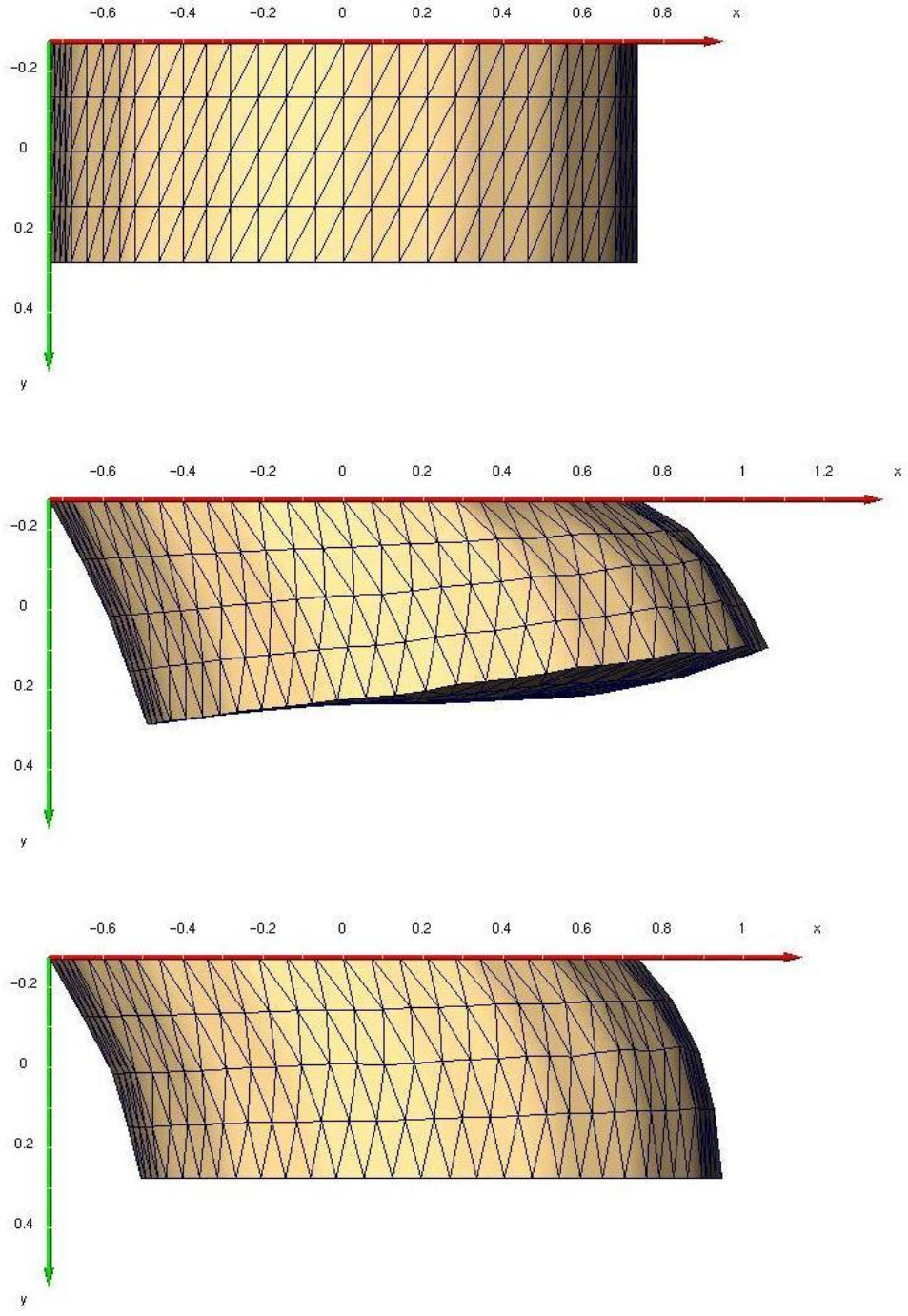

Figure 6.6: Top: undeformed cylindric object. Middle: deformation without sliding contact constraint. Bottom: deformation with sliding contact constraint on the cylinder bottom.

6.2 Soft Tissue Prediction in the CAS Planning

In this section, we present the experimental results of the soft tissue prediction within the craniofacial surgery planning. The experiments are carried out on the basis of geometrical models derived from preoperative CT data. Since postoperative tomographic data for the same patient are not available, we concentrate our efforts on the qualitative and indirect quantitative validation of the simulation outcome. For the qualitative evaluation, the surgeons are consulted. In order to quantify the modeling error, e.g., the error produced by the linear elastic approximation or the particular material description, one even do not need the "correct solution", since the modeling approach, as for instance the linear elastic FEM, implies the appropriate indicators for error detection itself.

Clinical case I. Large deformation. In the first example, the complete surgical planning of a juvenile patient with congenital mandibular hypoplasia, including the soft tissue prediction, is simulated, see Figure 6.7. The correcting surgical impact for this patient consists in the calus (mandible) distraction, which is shown in Figure 6.8. The total maximum displacement of bone structures for this patient amounts up to nearly 40mm, which cannot be classified as small deformation anymore. Such extremely large bone rearrangement is performed by surgeons stepwise over several months with the help of mechanical distractor device. Each step consists in an advancement of mandibula by approximately 1mm per day. Both the linear and non-linear elastic FEM are applied for the static prediction of the patient's postoperative appearance [50, 51].

Linear elastic approach. First, the deformation of facial tissue is computed stepwise with the linear elastic approach. The results of the soft tissue prediction for eight steps, each one associated with the mandible distraction of $0.4 - 0.6$cm, are shown in Figure 6.9. Since the calus distraction has not yet been completed, a direct comparison with the postoperative data is not possible. Thus, we are interested in the quantification of the error caused by the disregard of the geometrical non-linearity in the linear elastic approach. In order to quantify the linearization error, a criterion based on the monitoring of the maximum component of the linearized strain tensor $\epsilon = \max|\,\boldsymbol{\nabla}\mathbf{u}\,|$ is used, cf. (3.22). The correction of non-linear elasticity, i.e. the contribution to the non-linear terms of the strain tensor, is of the order $o(\epsilon^2)$. This means that ϵ indicates the *relative linearization error*. Further, the percentage of tetrahedrons with ϵ exceeding a certain threshold ϵ_i is monitored. The results of the monitoring of the relative linearization error in dependence on the intensity of the deformation (cf. Figure 6.9 (a-h)) are shown in Table 6.1 as well as in Figure 6.10 (top). We give an example of how to interpret these data. Consider the entry in the third row ($\epsilon_3 = 0.05$) and the e-th

Figure 6.7: A patient with congenital mandibular hypoplasia.

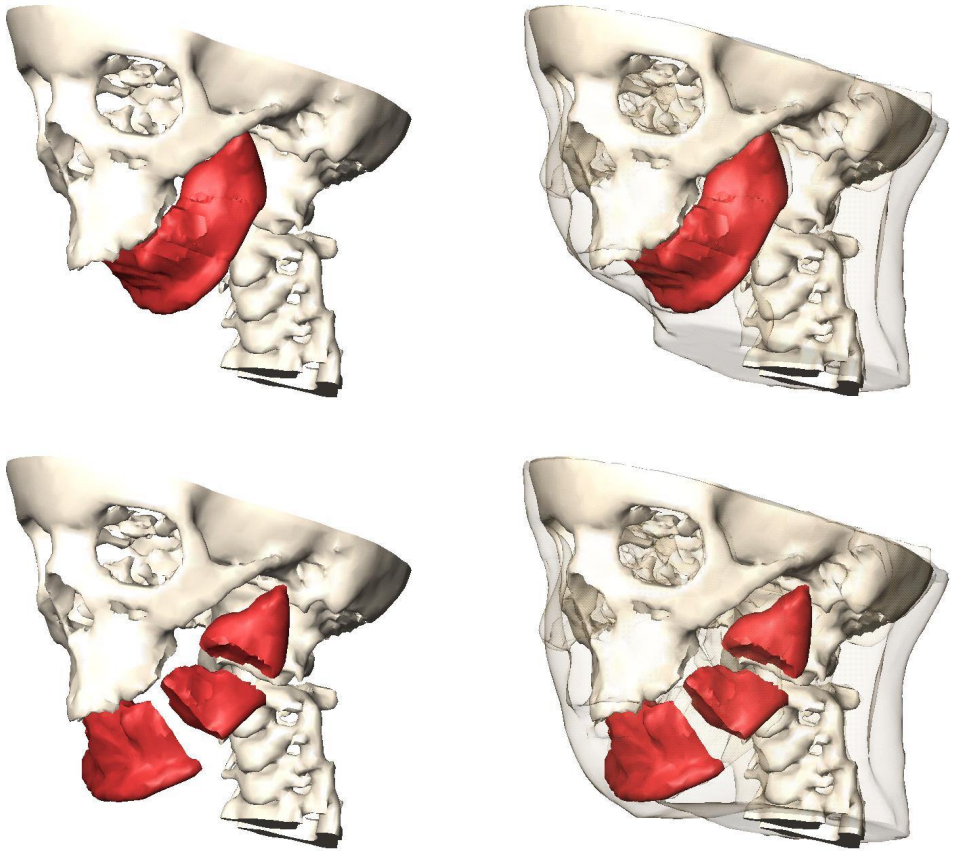

Figure 6.8: Simulation of mandible distraction.

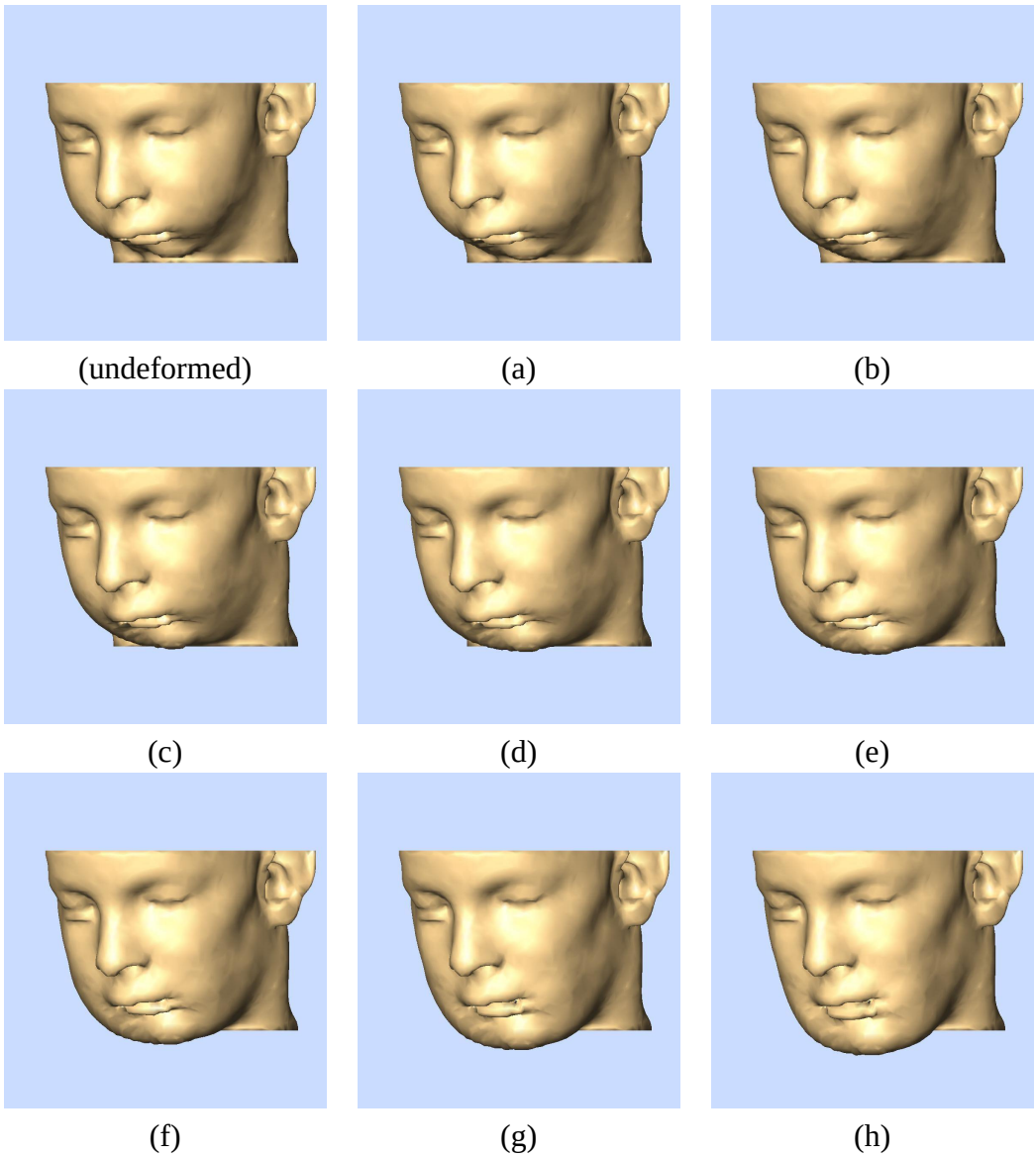

Figure 6.9: Resulting soft tissue deformation induced by the stepwise rearrangement of bone structures with maximal boundary displacements of: (a) 0.6cm, (b) 1.2cm, (c) 1.6cm, (d) 2.0cm, (e) 2.6cm, (f) 2.8cm, (g) 3.3cm, (h) 3.8cm.

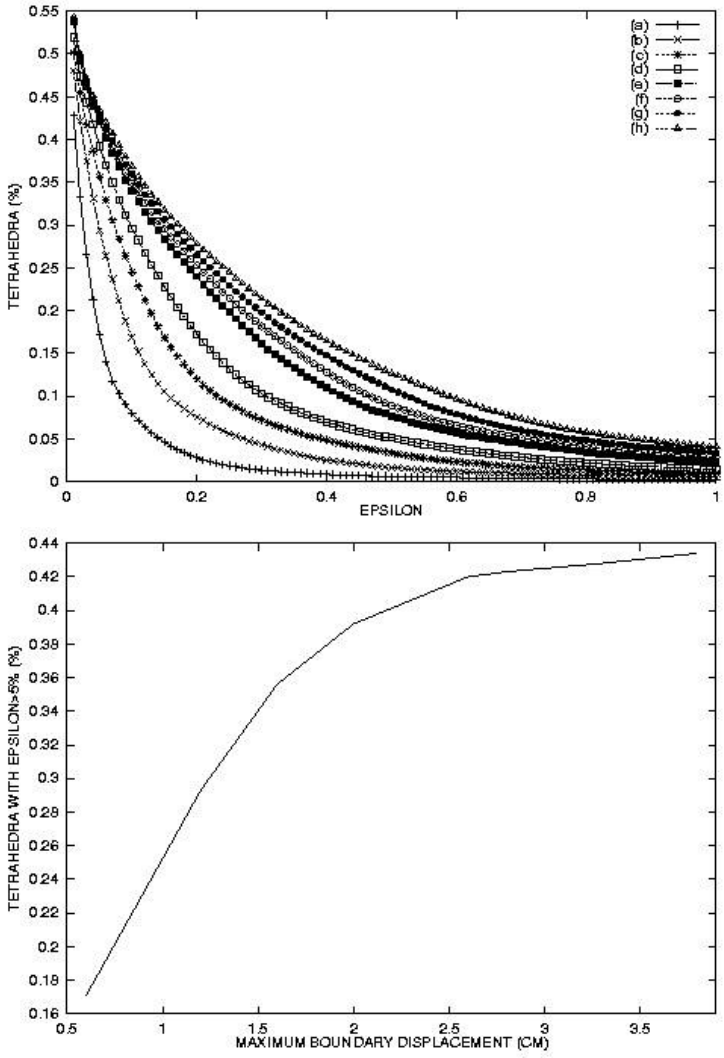

Figure 6.10: Top: distribution of the linearization error in dependence on the intensity of deformation, cf. Figure 6.9 (a-h). Bottom: percentage of tetrahedrons with $\epsilon > 5\%$ in dependence on maximum boundary displacements.

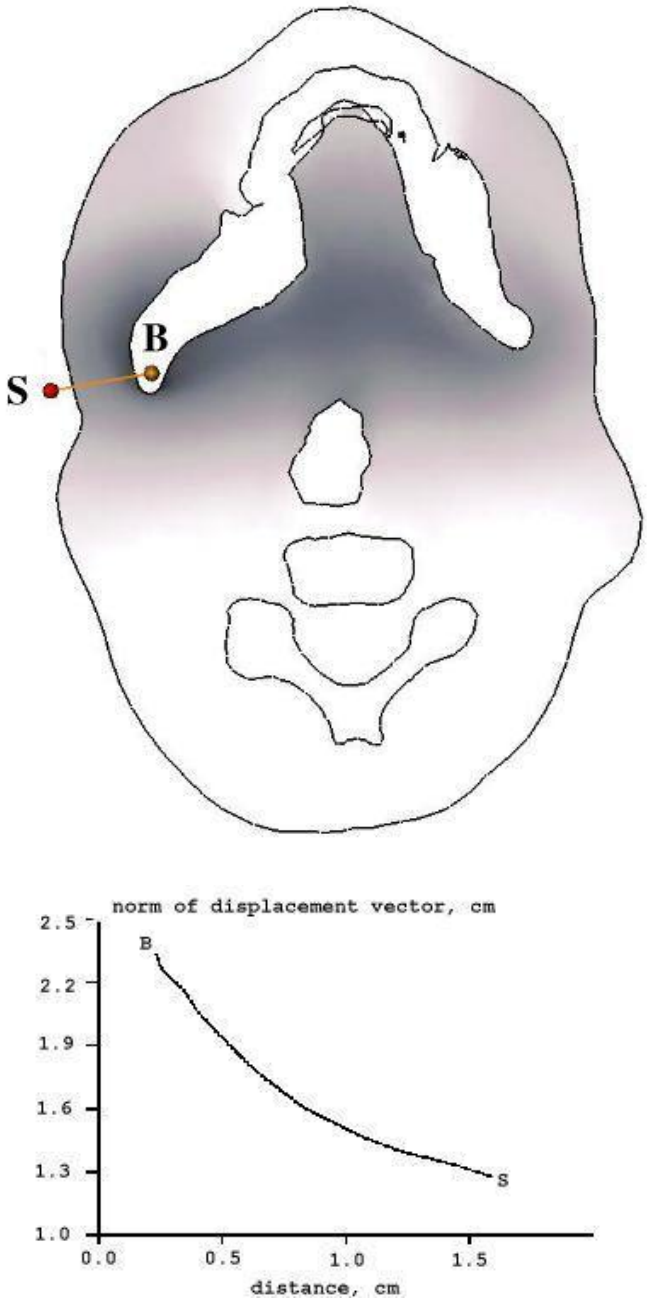

Figure 6.11: Top: 2D plain cut through a patient's head, grey-scale gradient indicates the spatial distribution of deformation represented by the norm of the displacement vectors. Bottom: decrease of the displacement field measured along the line probe: from the "source" B (bone) to S (skin).

Table 6.1: Validation of the linearization condition $\epsilon \ll 1$, cf. Figures 6.9 (a-h).

ϵ_i	percentage [%] of tetrahedrons with $\epsilon > \epsilon_i$							
	a	b	c	d	e	f	g	h
0.01	42.8	48.0	50.1	51.9	53.7	53.8	53.9	54.3
0.03	26.5	37.4	41.7	44.3	46.2	46.3	46.8	47.1
0.05	17.1	29.3	35.6	39.2	42.0	42.3	42.8	43.4
0.07	11.8	23.7	30.5	34.9	38.5	39.1	39.9	40.7
0.1	7.9	16.8	24.5	29.6	33.9	34.9	35.9	36.8
0.2	2.8	7.5	12.0	17.2	24.0	25.3	25.6	27.8
0.3	1.3	4.3	7.2	10.3	16.2	18.1	19.8	21.4
0.4	0.8	2.5	4.9	6.9	10.9	12.8	14.8	16.5
0.5	0.6	1.7	3.3	5.1	7.7	8.9	10.7	12.6
0.6	0.5	1.3	2.3	3.8	5.7	6.6	7.9	9.6
0.7	0.4	0.9	1.7	2.9	4.5	5.1	6.0	7.4
0.8	0.3	0.7	1.3	2.2	3.5	3.9	4.7	5.8
0.9	0.3	0.6	1.1	1.8	2.8	3.4	4.0	4.7
1.0	0.2	0.5	0.9	1.4	2.3	2.8	3.4	3.9

column (maximum boundary displacement of 2.6cm): 42.0%. This value means that in the case of the maximum boundary displacement of 2.6cm (cf. Figure 6.9e) for 42.0% of all tetrahedrons the relative linearization error lie over 5%, i.e. $\epsilon > 0.05$. In Figure 6.10 (bottom), the percentage of tetrahedrons with $\epsilon > 0.05$ in dependence on maximum displacement is depicted. The error curve shown in this diagram has no particular break-points, which would indicate the optimal step width for the linear calculation. In contrast, the strongest increase of the error-curve occurs on relative small displacements (duplication of error for maximum boundary displacements in the range of $[0.6, 1.6]$cm), which trivially means that the smaller step width produces the smaller linearization error. Consequently, the optimal step width as well as the corresponding precision of the linear elastic calculation are up to user. For the maximum deformation of 3.8cm (see Table 6.1 (h)), the relative linearization error amounts more than 5% for nearly half of all tetrahedra (43.4%). However, the analysis of spatial distribution of the linearization error shows that the largest error is concentrated inside of the patient's head in the direct vicinity of relocated bone structures. In contrast, on the facial surface, which is most important for an optical impression, one can hardly see any artifacts. This fact can be explained through the r^{-1} decrease of the displacement field with increasing distance from the source in$3D$, see Figure 6.11.

The computation of the deformation for a grid of 63.320 nodes (314.043 tetrahedra) via the linear elastic FEM took 1.8 minute (residual norm of PCG algorithm: 10^{-10}). The calculations are performed on an SGI Onyx II with 195MHz as well as on PC Pentium PIII with 600MHz.

Non-linear elastic approach. The linear elastic approximation of large deformations produces a substantial error caused by the disregard of the geometrical non-linearity. Thus, the non-linear elastic approach is applied for the soft tissue prediction. For this purpose, the adaptive non-linear elastic FEM is used. The results of the soft tissue prediction computed with the non-linear elastic approach vs the linear elastic one are shown in Figure 6.12. The deformation computed via the non-linear elastic approach is signifi cantly smaller in comparison with the outcome of the linear elastic FEM, which yields too large deformations, particularly in the chin area, see Figure 6.13.

By the computation of the non-linear elastic deformation some numerical problems occur. After the fi rst linear elastic step (cf. Figure 5.2) by higher order Newton iterations, the assembled system of equations sometimes becomes unsolvable due to the large condition number. The same problem concerning the iterative calculation of large deformations via the nonlinear elastic FEM has been reported in [95] in application to elastic image registration. We have found that the reason for such fatal errors lies in the strong dependence of the non-linear elastic calculation on the displacement gradient $\nabla \mathbf{u}$, which cannot be computed accurately if the initial grid contains degenerated elements and/or the inconsistent boundary conditions. In turn, the deeper reason for these failures lies in the violation of the topology-preserving condition (3.6), which can be used for the indication of the failure occurrence.

This problem concerns only the non-linear elastic FEM, since the successive computation of the displacement gradient is not required for the linear elastic FEM. The handling of this problem is not easy and basically can be classifi ed into two general groups of measures

(i) 'a priori' measures: quality control of the initial mesh and consistency proof of the applied boundary conditions,

(ii) 'a posteriori' measures: monitoring of the displacement gradient w.r.t. the topology-preserving condition.

In this work, 'a priori' measures, i.e. extensive checking and improvement of the quality of the initial mesh and the applied boundary conditions, already help

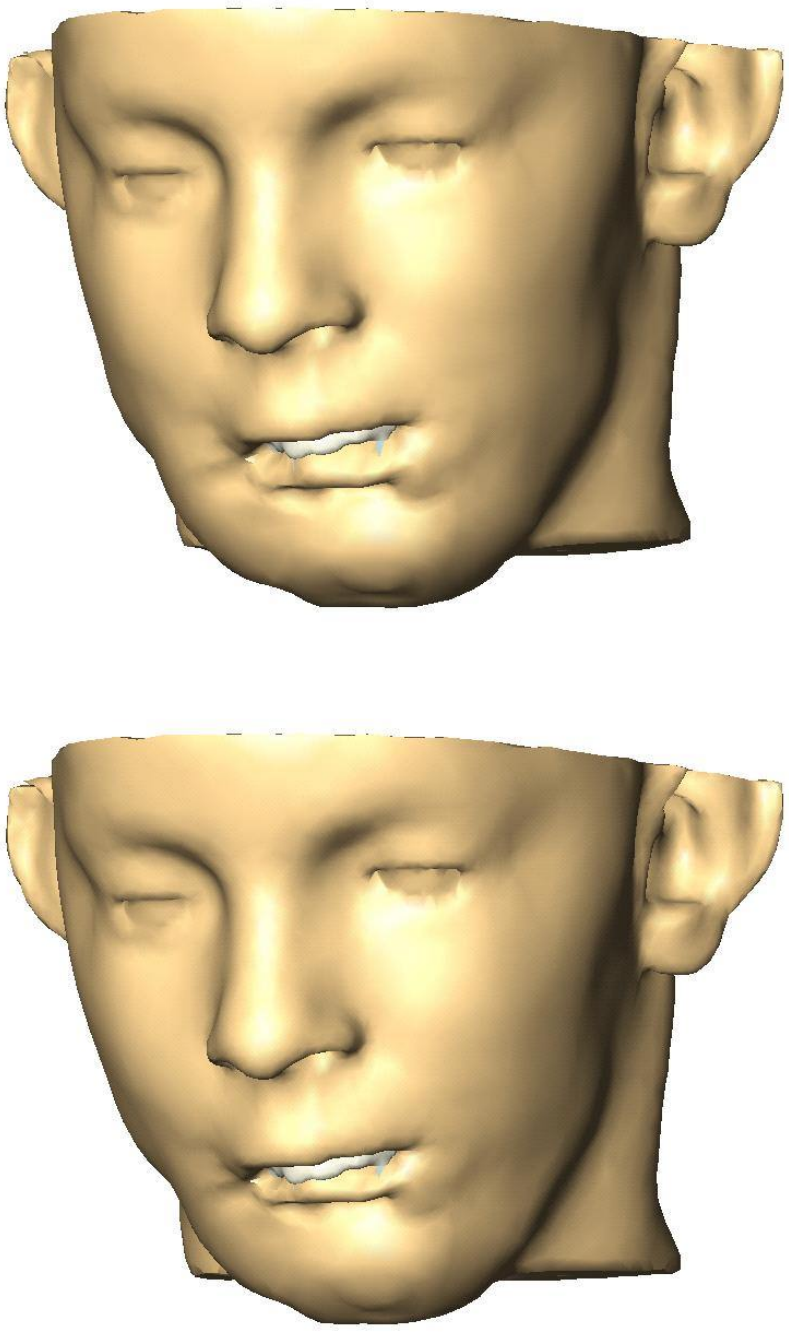

Figure 6.12: Simulation of large soft tissue deformation via the linear (top) and non-linear (bottom) elastic approach.

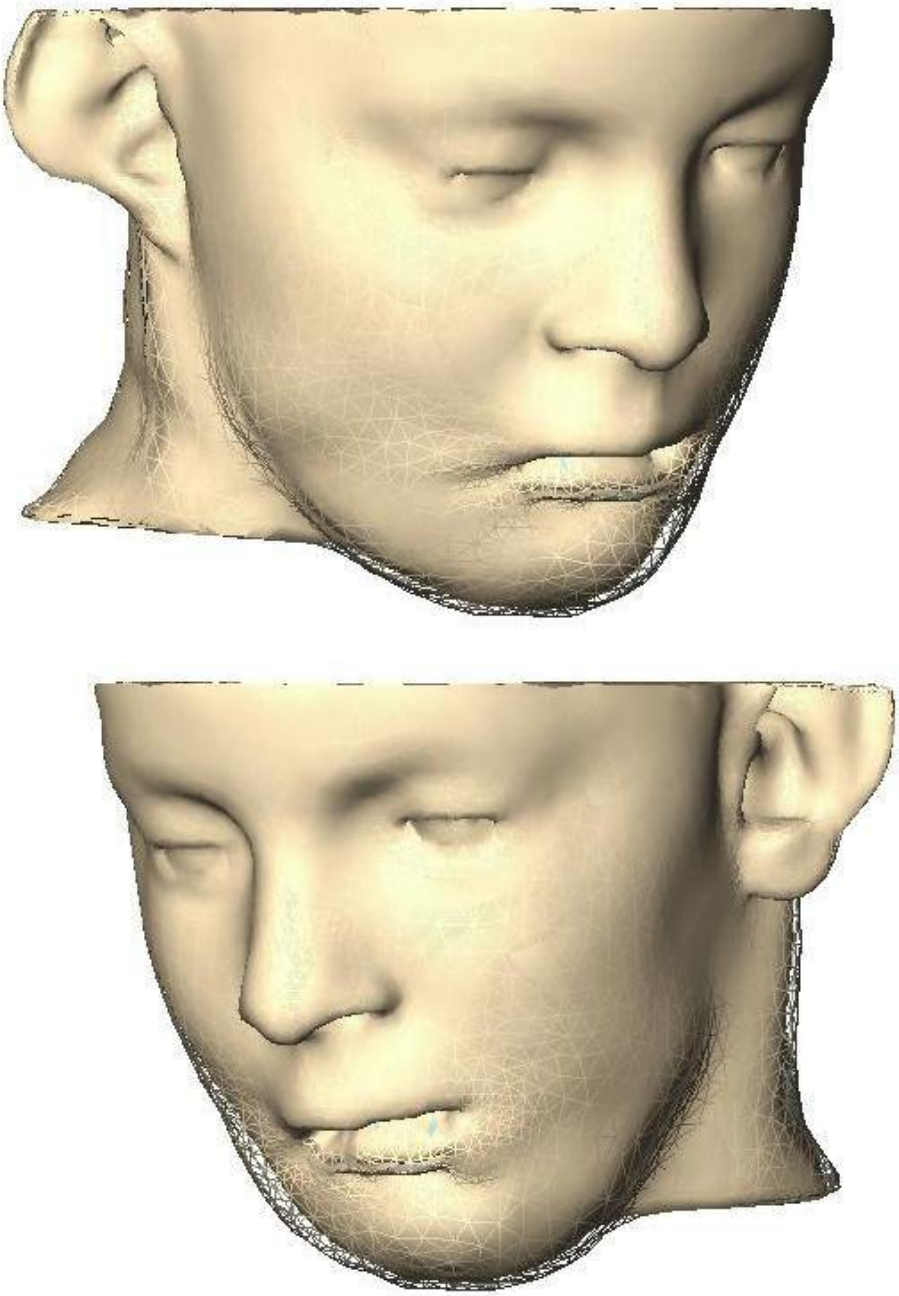

Figure 6.13: Comparison between the facial outline predicted by the linear (outer line mesh) and non-linear (inner shaded mesh) elastic model.

to fix the problem. However, the non-linear elastic approach appears generally more sensitive with respect to the small abnormalities of input data and thus less robust as the linear elastic FEM.

The performance of the adaptive non-linear elastic FEM is quite satisfactory. The calculation of the non-linear solution on the same grid took approximately 7 minutes, which corresponds to 4 iterations of the Newton method.

Clinical case II. Small deformation. In the next example, the postoperative appearance of a patient with maxillary retrognatism and mandibular prognatism is simulated, see Figure 6.15 (top). Figure 6.14 illustrates the simulation of the corrective surgical impact (bimaxillary osteotomy), which consists in an advancement of maxilla by 10mm and a set-back of mandibula by 12mm. The resulting soft tissue deformation is simulated with the linear and non-linear elastic FEM. In Figure 6.15 shows pre- and postoperative picture of the patient. In Figure 6.16, the comparison between the results of the linear and non-linear calculation is shown. Since the deformation in this case is relatively small, the linear solution matches well with the postoperative picture of the patient, see Figure 6.16 (1). However, a slight difference between postoperative and simulated profile outline in the nose area can be seen, Figure 6.16 (2). The non-linear solution yields better result, Figures 6.16 (3,4). Apparently, the reduction of this difference is due to the smaller displacement computed via the non-linear elastic FEM similar to the previously observed examples, cf. Figure 6.4 and 6.13. The remaining difference can be reduced by a higher stiffness of the nasal cartilage, which has not been taken into account by this simulation.

In this example, the linear elastic deformation for a grid of 106.166 nodes (504.112 tetrahedra) is computed in 2.9 minutes (residual norm of PCG algorithm: 10^{-10}) on the same hardware platform (SGI Onyx II with 195MHz as well as on PC Pentium PIII with 600MHz). The calculation of the non-linear elastic deformation took 9.3 minutes, which corresponds to 3 iterations of the Newton method.

Model sensitivity w.r.t. material parameters. Since soft tissue in our approach is modeled as a hyperelastic material, two elastic constants controlling the stiffness and the compressibility of each subdomain occupied by a different tissue layer are required.

Facial tissue stiffness. In the examples of static soft tissue prediction, facial tissue is firstly approximated as a 1-component homogeneous material. The simula-

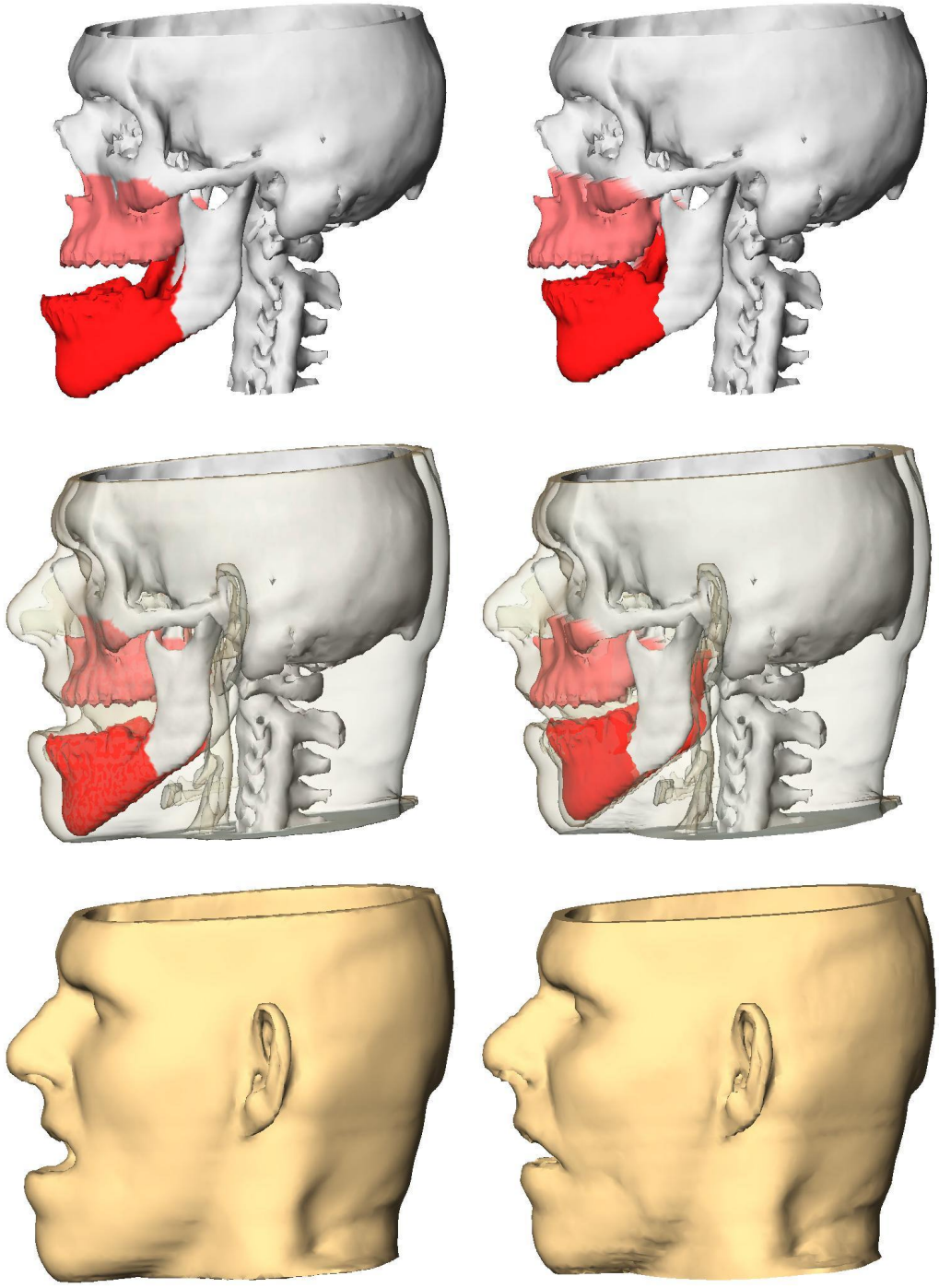

Figure 6.14: Simulation of bimaxillary osteotomy, including the soft tissue prediction.

Figure 6.15: A patient with maxillary retrognatism and mandibular prognatism. Top: preoperative picture. Bottom: postoperative picture.

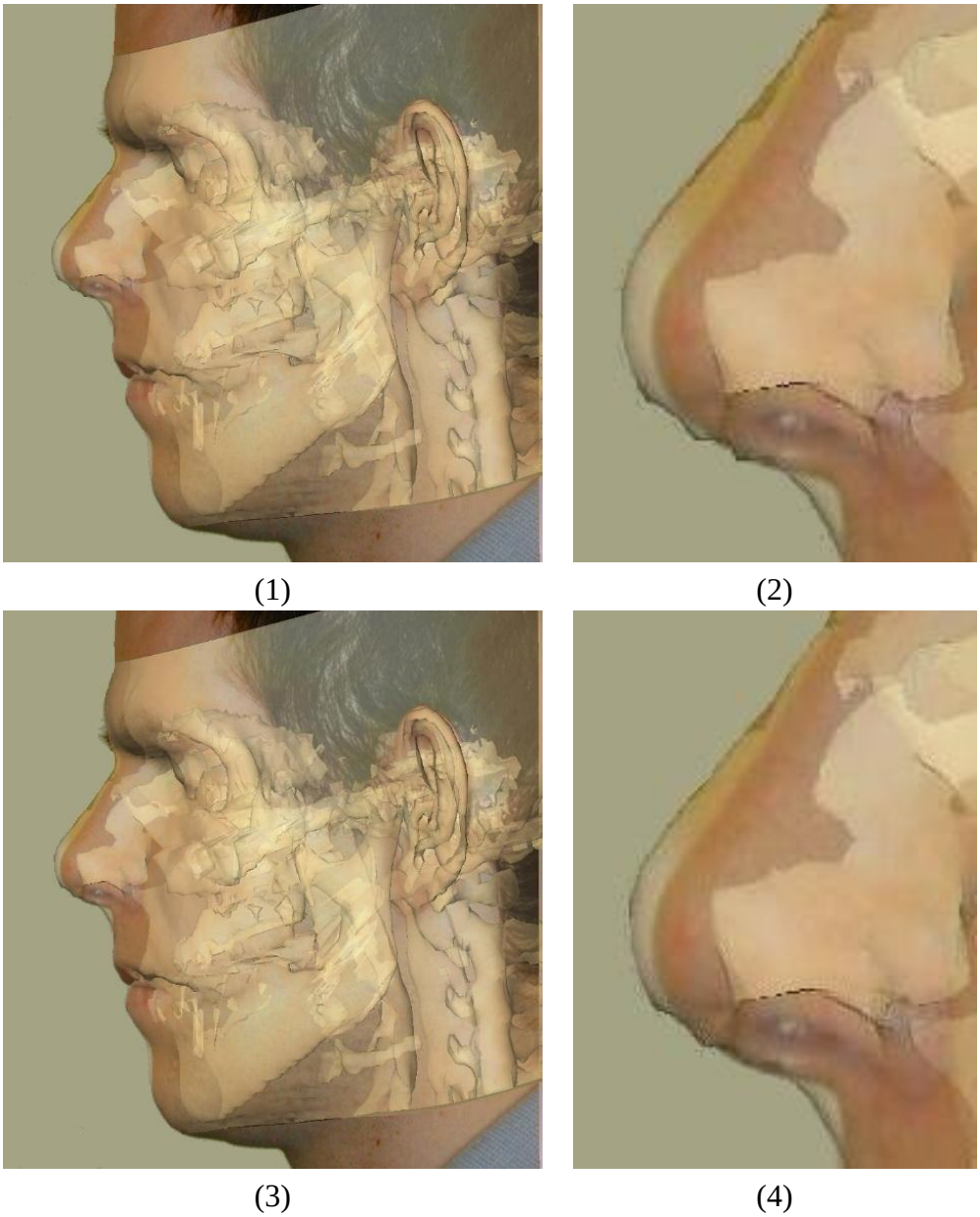

(1) (2)

(3) (4)

Figure 6.16: (1): validation of the linear elastic model, (2): nose area of (1), (3): validation of the non-linear elastic model, (4): nose area of (3).

tion results in the absence of explicitly given forces are not sensitive with respect to the Young modulus E describing the material stiffness. The simulations carried out with piecewise homogeneous approximation considering the different tissue regions have not shown any significant difference by the variation of the Young moduli of each particular tissue region in a "reasonable range" of values of E_i. However, the multi-layer model with different tissue stiffnesses becomes important for the modeling of facial expressions, where the deformations are induced by the impact of muscle forces, see Section 7.5.

Facial tissue compressibility. Quasi-incompressibility of soft tissue is modeled in this work with the Poisson ratio of up to $\nu = 0.45$. In previous sections, we have already addressed the problems concerning the numerical modeling of quasi-incompressible materials. Now, we validate the sensitivity of the modeling approach with respect to the Poisson ratio by the direct comparison of the simulation results for different $\nu \in [0,\, 0.45]$. In Figure 6.17, the results of the soft tissue prediction for $\nu = 0,\, 0.1,\, 0.2,\, 0.3,\, 0.4,\, 0.45$ are shown. Being basically present, the qualitative difference between the predicted facial surfaces can be visually registered between a high and low compressible material behavior only, cf. Figures 6.17 (a-c) and (d-f), respectively. Taking into account that the deformation simulated in this example is extremely large, the difference within the range of $\nu \in [0.3,\, 0.45]$ can be assumed neglectable and practically irrelevant for the qualitative evaluation of the postoperative outcome. From our findings, the Poisson ratio of $\nu = 0.4$ is a good compromise between the requirement of the constitutive modeling and the computational performance.

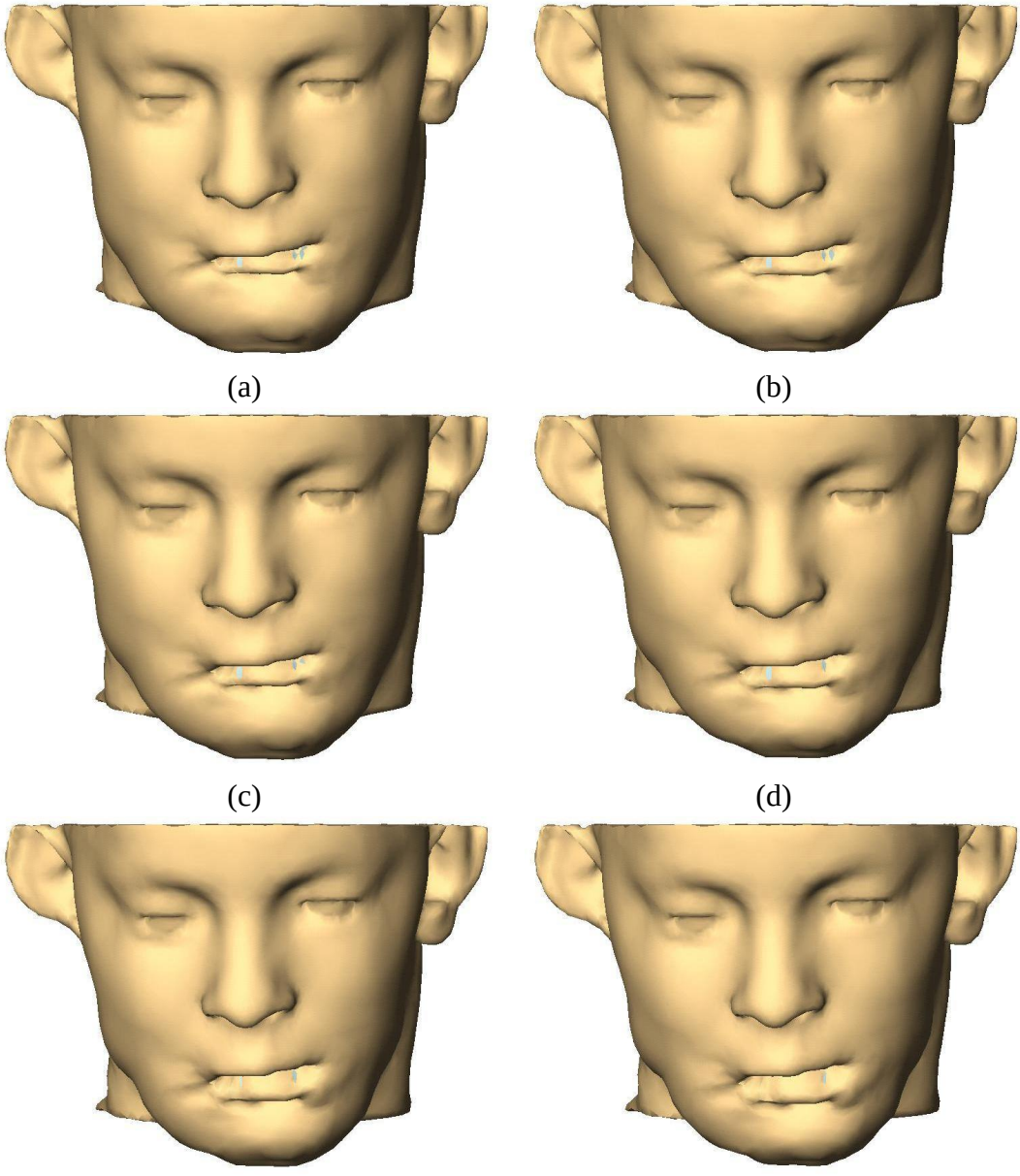

Figure 6.17: Results of soft tissue prediction for the Poisson ratio ν of (a): 0, (b): 0.1, (c): 0.2, (d): 0.3, (e): 0.4, (f): 0.45.